nature materials

Article

https://doi.org/10.1038/s41563-023-01622-0

Direct visualization of electronic transport in a quantum anomalous Hall insulator

Received: 4 May 2022

Accepted: 26 June 2023

Published online: 3 August 2023

Check for updates

G. M. Ferguson [1], Run Xiao [2], Anthony R. Richardella [2], David Low [1], Nitin Samarth [2] & Katja C. Nowack [1,3]

A quantum anomalous Hall (QAH) insulator is characterized by quantized Hall and vanishing longitudinal resistances at zero magnetic field that are protected against local perturbations and independent of sample details. This insensitivity makes the microscopic details of the local current distribution inaccessible to global transport measurements. Accordingly, the current distributions that give rise to transport quantization are unknown. Here we use magnetic imaging to directly visualize the transport current in the QAH regime. As we tune through the QAH plateau by electrostatic gating, we clearly identify a regime in which the sample transports current primarily in the bulk rather than along the edges. Furthermore, we image the local response of equilibrium magnetization to electrostatic gating. Combined, these measurements suggest that the current flows through incompressible regions whose spatial structure can change throughout the QAH regime. Identification of the appropriate microscopic picture of electronic transport in QAH insulators and other topologically non-trivial states of matter is a crucial step towards realizing their potential in next-generation quantum devices.

The quantization of electronic transport in quantum Hall insulators can be explained by a variety of microscopic models that predict markedly different local current distributions and potential landscapes. For example, some models emphasize the role of chiral edge states, which conduct along the sample perimeter[1]. Other work highlights the role of bulk currents driven by the Hall electric field[2]. Although most experiments are interpreted in terms of one of these microscopic models, an interplay between local band filling and external bias ultimately determines local current distribution. For the integer quantum Hall effect, imaging experiments have demonstrated the role of local Landau level filling in determination of both local sample properties and global transport coefficients[3–6]. In the context of the quantum anomalous Hall (QAH) effect[7–9], imaging experiments have focused on local magnetic order[10–13] and local conductivity[14]. However, direct measurements of transport current distribution have not been reported for the QAH effect or in any other quantum Hall system.

Here we use magnetic imaging to visualize current distribution in a QAH insulator. As schematically shown in Fig. 1a, we scan the pickup loop of a superconducting quantum interference device (SQUID) ~1 μm above the surface of a lithographically defined Hall bar fabricated from a magnetically doped topological insulator. The out-of-plane component of the stray magnetic field generated by the sample couples magnetic flux into the SQUID pickup loop[15], which we image with a spatial resolution of a few micrometres (Supplementary Section 1). We report the SQUID signal in units of the magnetic flux quantum Φ_0. We measure magnetic signals from the static magnetization, applied transport currents and magnetic response of the sample to changes in the applied top-gate voltage. To disentangle static magnetization from the latter two signals we modulate the voltage applied to the sample contacts or gate, respectively, at a finite frequency and detect the associated flux signal with a lockin amplifier.

Our measurements were carried out on a six-terminal Hall bar (device A) fabricated from a Cr-doped $(Bi,Sb)_2Te_3$ (BST) heterostructure

[1]Laboratory of Atomic and Solid-State Physics, Cornell University, Ithaca, NY, USA. [2]Department of Physics and Materials Research Institute, The Pennsylvania State University, University Park, PA, USA. [3]Kavli Institute at Cornell for Nanoscale Science, Cornell University, Ithaca, NY, USA. e-mail: kcn34@cornell.edu

https://doi.org/10.1038/s41563-023-01622-0

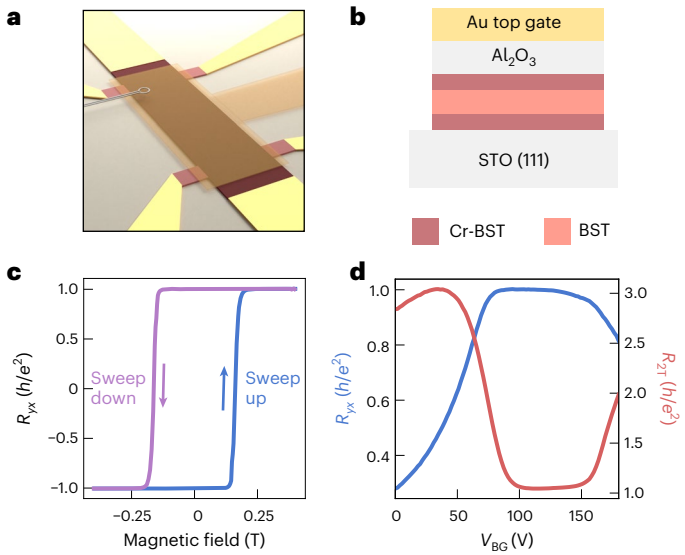

Fig. 1 | Magnetic imaging of a QAH effect sample. a, Schematic of a SQUID pickup loop imaging stray magnetic fields above a Hall bar sample of dimensions 200 × 75 μm^2. **b**, Cross-section of the sample. A four-quintuple layer (QL) of undoped BST is sandwiched between two three-QLs of Cr-doped BST. A gold layer insulated from the thin film by 40 nm of Al_2O_3 is used as a top gate extending beyond the Hall bar, as shown in **a**. V_{BG} is applied through the STO substrate. **c**, Hall resistance versus magnetic field at V_{BG} = 110 V showing a hysteresis loop. **d**, Hall resistance (R_{yx}, blue) and two-terminal resistance (R_{2T}, red) versus V_{BG} at zero magnetic field with the sample magnetized at +0.4 T.

grown on a $SrTiO_3$ (STO) substrate (Fig. 1b). The drain contact and its two adjacent voltage probes are shorted on-chip (Extended Data Fig. 1). Gating through the STO substrate allows us to tune the chemical potential through the gap. When the sample is magnetized, the transport coefficients reach a plateau with quantized values for a range of back-gate voltage, V_{BG} (Fig. 1c,d), indicating the QAH regime. Gate sweeps through a STO substrate often display history-dependent behaviour that probably arises from a charging effect in the STO[16–20]. Below, we use the values of the Hall resistance R_{yx} recorded with imaging data to account for these shifts and provide additional characterization in Supplementary Section 2. All imaging was performed in a zero external magnetic field after magnetization of the sample at either +0.4 or −0.4 T and with the microscope at a temperature of 45 mK unless otherwise noted. The data presented in the main text were acquired from the same Hall bar (device A). Data from a two-terminal sample (device B) fabricated from the same thin film, and a similar Hall bar (device C) fabricated from an additional thin film exhibiting the QAH effect, are included in Extended Data 3 and 4 and Supplementary Sections 3 and 4.

Current distribution in the QAH regime

To image transport currents we apply a bias voltage that oscillates between 0 and V_{bias} at a frequency of 140.5 Hz to the source contact with the drain contact grounded (Fig. 2c). The current flowing through the sample produces a stray magnetic field, which couples flux Φ_I into the SQUID pickup loop. Figure 2a shows an image of Φ_I with current $I_{a.c.}$ = 20 nA flowing through the channel at V_{BG} = 105 V. Here we define $I_{a.c.} = I^P_{a.c.}/\sqrt{2}$ where $I^P_{a.c.}$ is the amplitude of the sinusoidal part of the excitation (Methods). A lockin amplifier records the root mean squared (r.m.s.) value of the SQUID signal oscillating at 140.5 Hz in response to the applied current. Figure 2b shows the reconstructed current density (see Methods for details of the current reconstruction). Surprisingly, we found current flowing in the interior of the sample even though it was gated into the QAH regime.

In Fig. 2d,e we present line-cuts of Φ_I and the reconstructed x-component of current density, j_x, as a function of back-gate voltage for 15 nA through the sample. We focus on back-gate voltages at which transport is quantized and nearly dissipationless (Fig. 2f). We use a bias current of 25 nA or below, at which the QAH plateau is observed in transport and our measurements correspond to the linear response of the sample (Extended Data Figs. 3 and 4). Later in the paper we discuss measurements performed outside the dissipationless regime. The current distribution in device A depends on the back-gate voltage. At the lowest back-gate voltage, V_{BG} = 96 V, current density is located in a single strip within the Hall bar channel. As back-gate voltage is increased, this current density develops a depression in the centre of the channel and bifurcates into two separate strips of current. These strips move smoothly towards the edges of the channel as back-gate voltage increases. Simultaneously recorded measurements of R_{yx} and R_{2T} (Fig. 2f) show that the sample is tuned through the QAH regime as current density changes. We observed the same qualitative behaviour of current density in device B fabricated from the same thin film as device A (Extended Data Fig. 2). For device C (Supplementary Section 3) we found that the current distribution was in the interior of the sample and remained uniform throughout the QAH regime.

Within the QAH literature the quantization of transport coefficients is typically explained by dissipationless chiral edge states that transport current along the sample's perimeter. In our measurements most of the reconstructed current density profiles (Fig. 2e) are inconsistent with the current flowing in a narrow channel along sample edges. To reinforce this point using raw flux data, we consider three model current distributions (Fig. 2i,j) and convolve them with the imaging kernel of our SQUID to simulate the corresponding flux signal, Φ_{model} (Fig. 2h). The imaging kernel accounts for the Biot–Savart law and the geometry of the SQUID pickup loop (Methods). Φ_{model} can be directly compared with experimental Φ_I in Fig. 2d. Figure 2h–j shows that any edge conduction will appear as a sharp dip followed by a shallow peak in Φ_I near the sample edge. These signatures are absent in Fig. 2d, acquired on the low-V_{BG} side of the transport plateau. In Fig. 2g we compare Φ_I measured across one of the gold leads of the Hall bar with that observed in the QAH regime. Φ_I across the lead quantitatively agrees with a simulated flux profile assuming a uniform current density in the 75-μm-wide lead. In the QAH regime, Φ_I resembles the signal from the gold lead and is in quantitative agreement with a simulated flux profile for a uniform current density in a 40-μm-wide strip in the interior of the channel. This confirms that current is carried in the bulk of the sample at the corresponding back-gate voltage within the QAH regime.

Gate dependence of magnetization

Next we imaged the equilibrium magnetization of the sample, which we found showed how local band filling depends on back-gate voltage. Figure 3a shows an image of magnetic flux, $\Phi_{d.c.}$, produced by static magnetization with the sample magnetized at −0.4 T. From $\Phi_{d.c.}$ across the edges we estimate magnetization of ~10 μ_B nm^{-2} with μ_B as the Bohr magneton. This is within a factor of 2 of magnetization estimated from bulk measurements of 100-QL-thick films of Cr-doped BST[21].

To acquire the image shown in Fig. 3b we applied a small oscillating voltage, $V_{a.c.}$, to the top gate (Fig. 3c) and observed magnetization response. From images of Φ_V we reconstructed the corresponding change in magnetization, dM/dV_{TG} (Methods) for three back-gate voltages (Fig. 3d–f), which opposes the static magnetization of the sample. The signal was largely spatially uniform at V_{BG} = 55 V (Fig. 3d), whereas at V_{BG} = 110 V (Fig. 3e) we observed a substantial depression in dM/dV_{TG} in the channel interior and stronger signal near the sample edges. At V_{BG} = 150 V (Fig. 3f), dM/dV_{TG} was again spatially uniform but with a reduced amplitude compared with lower back-gate voltages. The total change across the back-gate voltage range was approximately 15% of magnetization at V_{BG} = 0 V and was also noticeable in our d.c. measurements.

https://doi.org/10.1038/s41563-023-01622-0

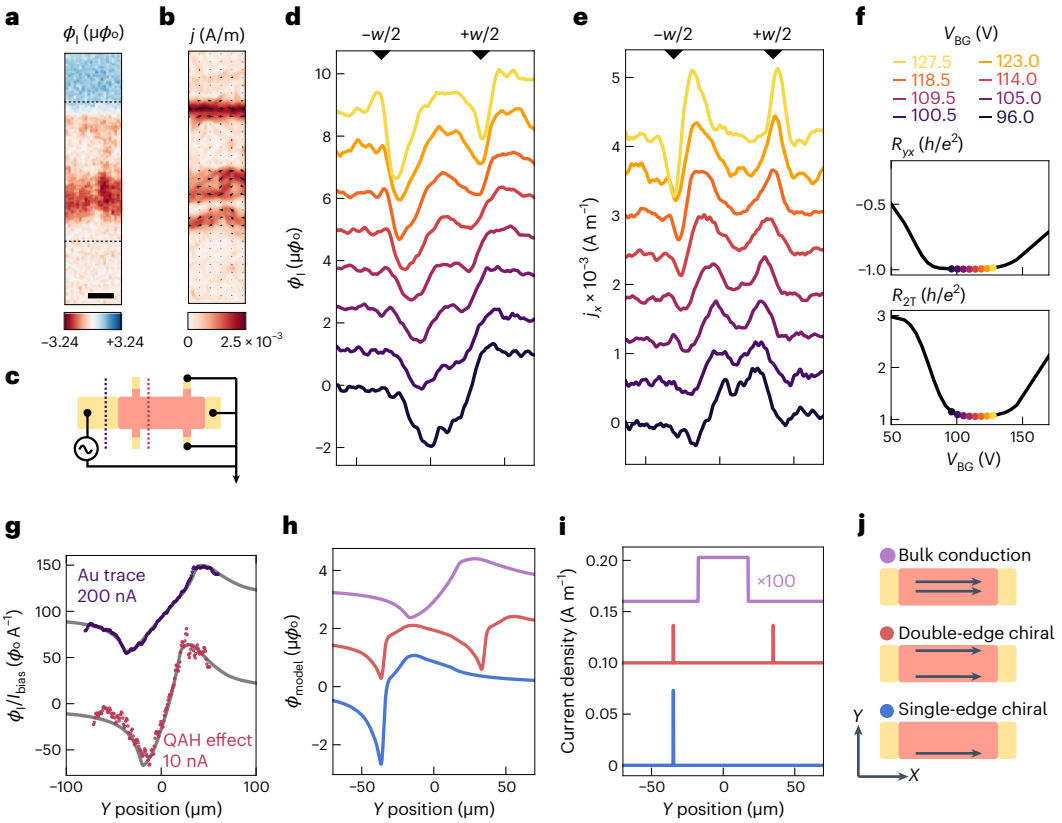

Fig. 2 | Bulk-dominated transport within the QAH regime. a–**c**, Images of magnetic flux, Φ_I (**a**) and reconstructed current density (**b**) with $I_{a.c.}$ = 20 nA applied in the channel by oscillating the source contact between 0 V and V_{bias} at a frequency of 140.5 Hz; shown schematically in **c**. Scale bar, 15 μm. **a**, Black dashed lines indicate the edges of the device. Data were acquired at V_{BG} = 105 V. **b**, Colour depth and arrows represent the magnitude and direction, respectively, of current density. **d**, Traces of Φ_I along the dashed red line in **c** for $I_{a.c.}$ = 15 nA as the sample is tuned through the QAH regime with the back gate. Traces are offset by 1.25 μΦ_0. Markers at the top indicate sample edges with w as the sample width. **e**, X-component of current density, j_x, reconstructed from **d**. Traces are offset by 3 × 10^{-4} A m^{-1}. **f**, R_{yx} and two-terminal resistance, R_{2T}, versus V_{BG} recorded simultaneously with each trace in **d**. **g**, Φ_I across a gold contact (purple, position indicated by leftmost line in **c**) and across the channel in the QAH regime with R_{yx} = 0.998 e^2/h at V_{BG} = 110 V (red). The QAH plateau has shifted by approximately 15 V compared with that shown in **d**–**f**. Traces are scaled by the applied current and offset for clarity. Grey curves are simulations of a 75- and 40-μm-wide uniform current profile for the Au and QAH effect trace, respectively. We note that the position of the QAH plateau has shifted by approximately 15 V between measurements in **d** and **g** (Supplementary Section 2). **h**, Simulated magnetic flux profiles, Φ_{model}, for three simple model current distributions. **i**, Model densities corresponding to flux profiles in **h**. **j**, Schematic depiction of the three model current distributions.

The gate dependence of dM/dV_{TG} is strongly correlated with both electrical transport measurements and transport current distribution. To capture how dM/dV_{TG} changes in detail we measured line traces over the width of the sample as a function back-gate voltage. The reconstructed dM/dV_{TG} is shown in Fig. 3h. Starting at around V_{BG} = 75 V, dM/dV_{TG} showed a shallow local minimum near the centre of the channel followed by a gradual increase (Fig. 3d). With increasing back-gate voltage this structure spread towards the edges of the sample, giving rise to the wedge-shaped feature seen in Fig. 3h. R_{yx} and two-terminal resistance R_{2T} exhibited a plateau of h/e^2 (h is Planck's constant and e is the elementary charge) throughout the back-gate voltage range in which this feature appeared (Fig. 3i) The bifurcation in transport current distribution (Fig. 2e) began at a voltage similar to the wedge-shaped region in dM/dV_{TG}, and transport current appeared to flow roughly in regions in which dM/dV_{TG} changed. Taken together, these observations suggest that the gate-dependent behaviour of dM/dV_{TG}, R_{yx} and j_x can be traced to a common microscopic origin. Furthermore, the transport data indicate that the chemical potential μ is in the valence band at V_{BG} < 75 V and in the conduction band at V_{BG} > 150 V. At these back-gate voltages, dM/dV_{TG} is largely uniform but the amplitude is dependent on whether μ is in the valence or conduction band. Based on this, we use dM/dV_{TG} in Fig. 3h as a spatially resolved indicator of local band filling.

We now briefly discuss the potential origins of the observed dM/dV_{TG}. First, an orbital contribution, M_{orb}, to magnetization depends on band filling and the distribution of Berry curvature within the conduction and valence bands[22]. When μ is in the gap, dM_{orb}/dV is predicted to be $\sigma_{xy} \times \partial\mu/\partial(eV_{TG})$ (refs. 23–25). The maximum observed amplitude is approximately 2% of $\sigma_{xy} = e^2/h$, which could be due to localized mid-gap states limiting $\partial\mu/\partial(eV_{TG})$, which is how efficiently the top gate modulates chemical potential. Quantitative estimation of dM_{orb}/dV, when μ is either in the conduction or valence band, requires detailed knowledge of Berry curvature and $\partial\mu/\partial(eV_{TG})$. Second, magnetization of Cr-dopants may depend on charge carrier density. A substantial Van Vleck spin susceptibility was previously proposed to mediate ferromagnetic coupling between magnetic dopants. More recent studies, however, suggest that additional mechanisms may contribute to coupling, including a hole-mediated RKKY interaction[12] and magnetic exchange interactions mediated by dopant impurity bands[26]. While ferromagnetic order clearly persists in the absence of free carriers, some changes in magnetic properties with carrier density have been reported[12,27]. Although clarification of different contributions to dM/dV_{TG} requires further work, dM/dV_{TG} clearly indicates the transition from filling the valence band to filling the conduction band.

https://doi.org/10.1038/s41563-023-01622-0

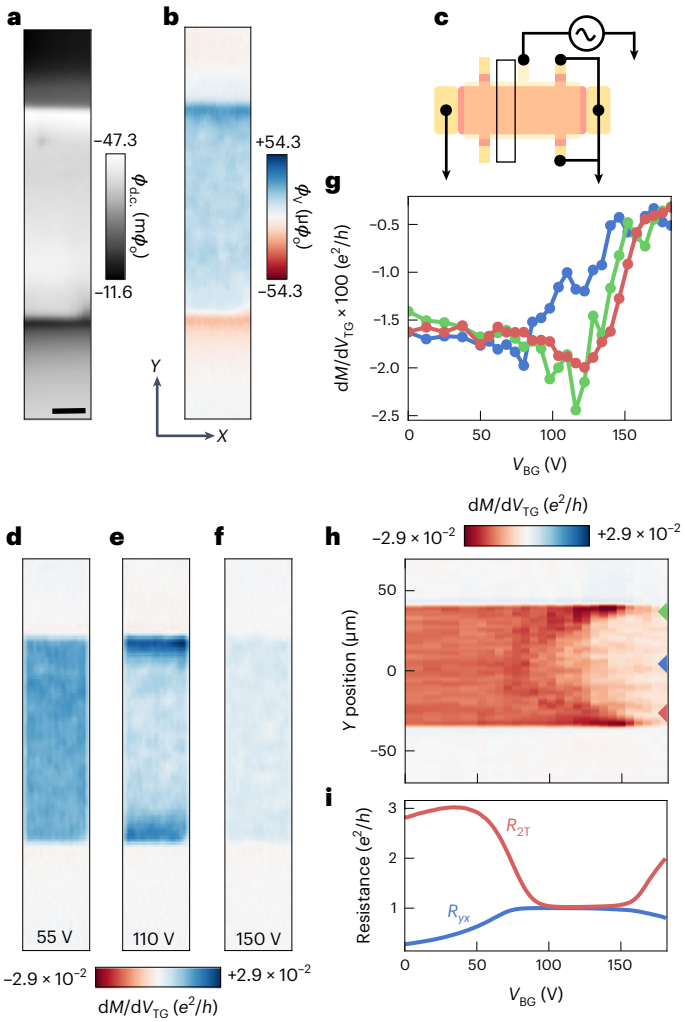

Fig. 3 | Identification of local band filling through gate-induced magnetic response. a, Image of static magnetic flux, $\Phi_{d.c.}$, with the sample magnetized at −0.4 T. Scale bar, 10 μm. **b**, Image taken from the same area of magnetic response, Φ_V, for modulation of top-gate voltage, V_{TG}, with $V_{a.c.}$ = 240 mV at 140.5 Hz while both source and drain contacts are grounded. **c**, Diagram of system used. **d**, Response of magnetization, dM/dV_{TG}, reconstructed from Φ_V in **b**. **e**,**f**, dM/dV_{TG} at additional V_{BG}. **g**, dM/dV_{TG} versus V_{BG} at the Y positions indicated in **h**. **h**, Line traces of dM/dV_{TG} versus V_{BG} with the sample magnetized at +0.4 T. **i**, corresponding Hall and two-terminal resistances, R_{yx} and R_{2T}, respectively.

Microscopic model

Our observations are consistent with a model of electronic transport developed for the integer quantum Hall effect in which dissipationless transport current is driven by transverse electric fields in insulating, incompressible regions of the sample[5]. The spatial structure of the incompressible regions is primarily dictated by electrostatics: interplay between intrinsic carrier density, confining potential, trapped charges, gate voltages and screening properties of the charge carriers determines local carrier density and band filling within the sample. In particular, when the electronic spectrum is gapped some electrostatic energy may be saved through the formation of incompressible regions in the sample interior in which the chemical potential remains in the gap[28]. In the context of the integer quantum Hall effect, the relevant energy gap is Landau level splitting. In the QAH effect the size of the gap is determined by the magnetization of the sample and details of band structure[8]. When σ_{xx} vanishes and σ_{xy} is quantized, the Hall electric field drives a dissipationless current in these incompressible strips. In this scenario the position and geometry of the incompressible strips play a central role in local potential and current distribution within the sample.

To compare this scenario with our results we replotted dM/dV_{TG} in Fig. 4a over a range of V_{BG} centred around the gap. Incompressible strips are expected to form in regions where the chemical potential transitions from the valence band minimum and conduction band maximum. We therefore identified the transition region between the strong dM/dV_{TG} signal from the valence band and the weaker dM/dV_{TG} signal from the conduction band as the range of positions and V_{BG} where the sample is incompressible. We mark this region with a dashed line in Fig. 4a. In Fig. 4c we show a normalized current density, $j_N = j_x/(\max\{j_x\} - \min\{j_x\})$, for each V_{BG} to highlight where the sample supports a finite current density. We first focus on the range of back-gate voltages above the black marker seen in Fig. 4c, where dissipation in the sample is low, before returning to lower back-gate voltages below. In Fig. 4a,c we plot the data as a function of $V_{BG} - V_{Off}$ to account for a shift in the position of the QAH plateau between the two measurements. V_{Off} is the back-gate voltage that maximizes R_{yx} for each measurement (Extended Data Fig. 6). We found that regions with a finite current density closely tracked the geometry of the regions identified as incompressible from dM/dV_{TG}. This suggests that the transverse electric field drives a dissipationless Hall current in the incompressible regions in our sample. In Fig. 4b we show a schematic corresponding to local band filling as a function of V_{BG} inferred from our data. In Fig. 4d,e we show corresponding real-space diagrams of local band filling for two different back-gate voltages.

Within this model it is the anomalous velocity of carriers in the topologically non-trivial valence band, rather than edge states, that supports quantized transport. Although bulk transport dominates in our samples, in general both edge states and bulk may contribute to transport in quantum Hall insulators, with the details determined by the electrostatic configuration of the sample[2,29,30]. In our experiments we cannot definitively exclude a small fraction of the current flowing along the sample edge. Similarly, we cannot rule out a long, narrow conducting pathway that winds through the bulk substantially below our spatial resolution (see Supplementary Section 6 for discussion of these scenarios). A complete understanding of transport in QAH insulators will require investigations spanning several different materials systems, device geometries and experimental techniques. For example, direct comparison between local electrostatic properties such as local compressibility, transport current distributions and global electrical transport coefficients measured on the same sample could directly clarify the relationship between current density and incompressible regions in the sample.

Imaging outside the dissipationless regime

Finally we discuss the currents in Fig. 4c that appear to be circulating the sample at back-gate voltages for which transport is not quantized (Extended Data Fig. 3). The associated flux signals exceed the signal expected from the transport current by approximately one order of magnitude, do not invert with the sign of the applied bias and are nonlinear (Extended Data Fig. 7 and Supplementary Section 5). This suggests that the signals originate from bias-induced heating and not directly from magnetic fields produced by the transport current. Similarly, the counterflowing current visible in Figs. 2e and 4b has a nonlinear dependence on bias current and merges with heating-induced signals as the back-gate voltage tunes the sample out of the QAH regime, suggesting that these signals are likewise due to heating. The spatial structure, sign and amplitude of the signals outside the QAH regime are consistent with bias-induced heating causing demagnetization in the order of 0.1%. Substantial heating of the electron system is expected outside the QAH regime, where a finite σ_{xx} causes non-zero power dissipation in the sample (Fig. 4f). At millikelvin temperatures, where electron–phonon coupling is weak, small currents can generate

https://doi.org/10.1038/s41563-023-01622-0

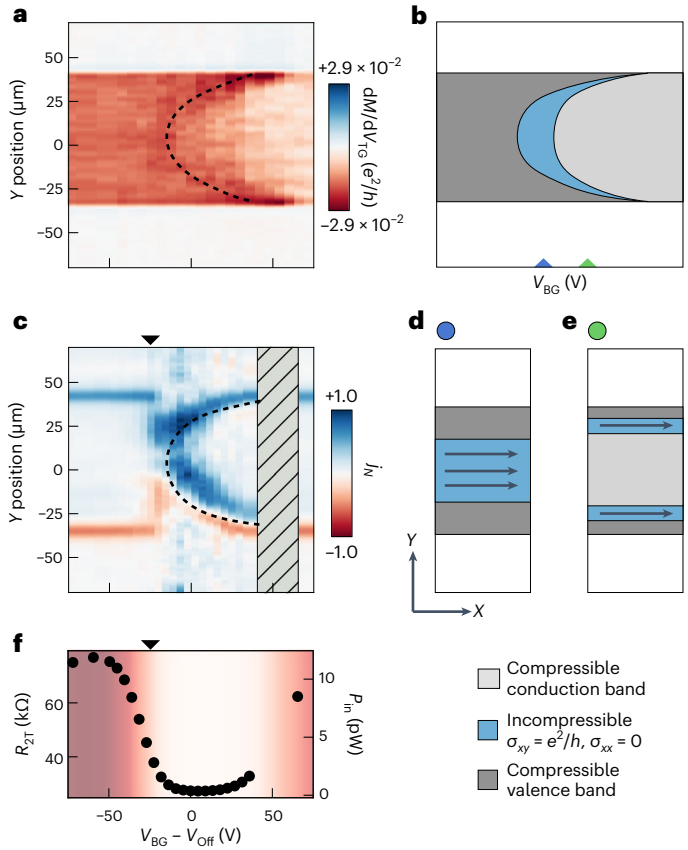

Fig. 4 | Microscopic model of transport in the QAH regime. a, dM/dV_{TG} from Fig. 2g. **b**, Schematic of inferred real-space band filling in the channel as back-gate voltage changes. **c**, Current density as in Fig. 2e but normalized and over a wider V_{BG} range. Each line is normalized to vary between −1.0 and 1.0 on the colour scale. For V_{BG} below the black marker, heating-induced signals become dominant (see main text). The back-gate voltage is shifted by V_{Off}, determined as V_{BG} at which R_{yx} is maximum in each measurement, allowing us to plot **a**,**c**,**f** on the same horizontal axis. Dashed black lines are visual guides highlighting the same regions in **a**,**b**. No data are available for values of V_{BG} indicated by the grey area. **d**,**e**, Real-space diagrams of compressible and incompressible regions in the sample at the two back-gate voltages indicated in **c**. A dissipationless current may flow in the incompressible regions. Both cases show QAH effect but current distribution varies. **f**, R_{2T} (left axis) and power dissipated in the sample, P_{in} (right axis), versus V_{BG}.

large differences between electron and lattice temperatures[31,32]. We observed these signals, which we attribute to current-induced heating for V_{BG} below and above (Extended Data Fig. 8) the QAH regime, as well as at bias currents exceeding 30 nA throughout the whole back-gate voltage range, and in a Hall bar (device D) fabricated from a Cr-doped Sb_2Te_3 thin film that does not exhibit the QAH effect. This indicates that demagnetization is linked to dissipation rather than to the QAH effect. Coupling between magnetization and electron temperature may also be important in previous studies of magnetically doped topological insulators[10,33,34] where dissipation influenced the dynamics of magnetization. A detailed characterization of flux signals and electronic transport as a function of bias current for devices A, C and D is provided in the Extended Data and Supplementary Information.

Local measurements of dissipation in the integer quantum Hall effect reveal so-called hot spots in the corner of contacts at which the current is assumed to enter the device[35,36]. If local heating reduced magnetization in our sample, hot spots should also have been visible in magnetic imaging when we imaged the contact area of the Hall bar. We indeed saw signals consistent with local demagnetization near the corner of the source contact when the sample was in the QAH regime (Extended Data Fig. 7). When magnetization was reversed this hot spot moved to the opposite corner, consistent with the motion of hot spots in the quantum Hall effect when magnetic field is reversed.

Outlook

Macroscopic transport measurements can average over the sample volume in unexpected ways[4,37–42]. In quantum Hall systems this problem is compounded by strong real-space variations in the conductivity tensor. Here we provide an example in which currents in the sample bulk can give rise to the QAH effect. In addition, we observed variations between samples indicating that current distributions in the QAH regime are not universal. Our results underscore the importance of local probes in the development of microscopic models of conduction in topologically non-trivial systems. We note that the current distributions observed here bear a striking resemblance to those inferred from local measurements of Hall potential in the integer quantum Hall effect[5,43]. Taken together, these local imaging experiments are consistent with a unified picture for conduction in quantum Hall systems. Further support for this scenario is found in detailed analysis of electrical transport data on QAH samples[44]. Developing an accurate microscopic picture of transport in these topological materials is another step towards a detailed understanding of the breakdown of transport quantization and the integration of the materials into quantum devices with novel functionality[45,46].

Online content

Any methods, additional references, Nature Portfolio reporting summaries, source data, extended data, supplementary information, acknowledgements, peer review information; details of author contributions and competing interests; and statements of data and code availability are available at https://doi.org/10.1038/s41563-023-01622-0.

References

1. Büttiker, M. Absence of backscattering in the quantum Hall effect in multiprobe conductors. *Phys. Rev. B* **38**, 9375–9389 (1988).
2. Thouless, D. Edge voltages and distributed currents in the quantum Hall effect. *Phys. Rev. Lett.* **71**, 1879–1882 (1993).
3. Lai, K. et al. Imaging of coulomb-driven quantum Hall edge states. *Phys. Rev. Lett.* **107**, 176809 (2011).
4. Cui, Y.-T. et al. Unconventional correlation between quantum Hall transport quantization and bulk state filling in gated graphene devices. *Phys. Rev. Lett.* **117**, 186601 (2016).
5. Weis, J. & Von Klitzing, K. Metrology and microscopic picture of the integer quantum Hall effect. *Philos. Trans. A Math. Phys. Eng. Sci.* **369**, 3954–3974 (2011).
6. Marguerite, A. et al. Imaging work and dissipation in the quantum Hall state in graphene. *Nature* **575**, 628–633 (2019).
7. Haldane, F. D. M. Model for a quantum Hall effect without Landau levels: condensed-matter realization of the 'parity anomaly'. *Phys. Rev. Lett.* **61**, 2015–2018 (1988).
8. Yu, R. et al. Quantized anomalous Hall effect in magnetic topological insulators. *Science* **329**, 61–64 (2010).
9. Chang, C.-Z. et al. Experimental observation of the quantum anomalous Hall effect in a magnetic topological insulator. *Science* **340**, 167–170 (2013).
10. Lachman, E. O. et al. Visualization of superparamagnetic dynamics in magnetic topological insulators. *Sci. Adv.* **1**, e1500740 (2015).
11. Lachman, E. O. et al. Observation of superparamagnetism in coexistence with quantum anomalous Hall $C = \pm 1$ and $C = 0$ Chern states. *NPJ Quantum Mater.* **2**, 70 (2017).
12. Wang, W. et al. Direct evidence of ferromagnetism in a quantum anomalous Hall system. *Nat. Phys.* **14**, 791–795 (2018).

13. Tschirhart, C. et al. Imaging orbital ferromagnetism in a moiré Chern insulator. *Science* **372**, 1323–1327 (2021).
14. Allen, M. et al. Visualization of an axion insulating state at the transition between 2 chiral quantum anomalous Hall states. *Proc. Natl Acad. Sci. USA* **116**, 14511–14515 (2019).
15. Huber, M. E. et al. Gradiometric micro-SQUID susceptometer for scanning measurements of mesoscopic samples. *Rev. Sci. Instrum.* **79**, 053704 (2008).
16. Caviglia, A. et al. Electric field control of the $LaAlO_3/SrTiO_3$ interface ground state. *Nature* **456**, 624–627 (2008).
17. Bell, C. et al. Dominant mobility modulation by the electric field effect at the $LaAlO_3/SrTiO_3$ interface. *Phys. Rev. Lett.* **103**, 226802 (2009).
18. Biscaras, J. et al. Limit of the electrostatic doping in two-dimensional electron gases of $LaXO_3$ (X = Al, Ti)/$SrTiO_3$. *Sci. Rep.* **4**, 6788 (2014).
19. Mikheev, E., Rosen, I. T. & Goldhaber-Gordon, D. Quantized critical supercurrent in $SrTiO_3$-based quantum point contacts. *Sci. Adv.* **7**, eabi6520 (2021).
20. Yin, C. et al. Electron trapping mechanism in $LaAlO_3/SrTiO_3$ heterostructures. *Phys. Rev. Lett.* **124**, 017702 (2020).
21. Kandala, A., Richardella, A., Kempinger, S., Liu, C.-X. & Samarth, N. Giant anisotropic magnetoresistance in a quantum anomalous Hall insulator. *Nat. Commun.* **6**, 7434 (2015).
22. Xiao, D., Chang, M.-C. & Niu, Q. Berry phase effects on electronic properties. *Rev. Mod. Phys.* **82**, 1959–2007 (2010).
23. Streda, P. & Smrcka, L. Thermodynamic derivation of the Hall current and the thermopower in quantising magnetic field. *J. Phys. C Solid State Phys.* **16**, L895–L899 (1983).
24. Widom, A. Thermodynamic derivation of the Hall effect current. *Phys. Lett. A* **90**, 474–474 (1982).
25. Kohmoto, M., Halperin, B. I. & Wu, Y.-S. Diophantine equation for the three-dimensional quantum Hall effect. *Phys. Rev. B* **45**, 13488–13493 (1992).
26. Tcakaev, A. et al. Comparing magnetic ground-state properties of the v-and cr-doped topological insulator $(Bi, Sb)_2Te_3$. *Phys. Rev. B* **101**, 045127 (2020).
27. Checkelsky, J. G., Ye, J., Onose, Y., Iwasa, Y. & Tokura, Y. Dirac-fermion-mediated ferromagnetism in a topological insulator. *Nat. Phys.* **8**, 729–733 (2012).
28. Chklovskii, D., Shklovskii, B. I. & Glazman, L. Electrostatics of edge channels. *Phys. Rev. B* **46**, 4026–4034 (1992).
29. Van Son, P. & Klapwijk, T. Current contacts and current distribution in the quantum Hall effect. *Europhys. Lett.* **12**, 429–434 (1990).
30. Hirai, H. & Komiyama, S. Ratio between edge and bulk currents in the quantum Hall effect. *Phys. Rev. B* **49**, 14012–14015 (1994).
31. Roukes, M. L., Freeman, M., Germain, R., Richardson, R. & Ketchen, M. Hot electrons and energy transport in metals at millikelvin temperatures. *Phys. Rev. Lett.* **55**, 422–425 (1985).
32. Wellstood, F., Urbina, C. & Clarke, J. Hot-electron effects in metals. *Phys. Rev. B* **49**, 5942–5955 (1994).
33. Liu, M. et al. Large discrete jumps observed in the transition between chern states in a ferromagnetic topological insulator. *Sci. Adv.* **2**, e1600167 (2016).
34. Rodenbach, L. K. et al. Bulk dissipation in the quantum anomalous Hall effect. *APL Mater.* **9**, 081116 (2021).
35. Klass, U., Dietsche, W., Von Klitzing, K. & Ploog, K. Fountain-pressure imaging of the dissipation in quantum-Hall experiments. *Phys. Rev. B Condens. Matter* **169**, 363–367 (1991).
36. Klass, U., Dietsche, W., von Klitzing, K. & Ploog, K. Image of the dissipation in gated quantum Hall effect samples. *Surf. Sci.* **263**, 97–99 (1992).
37. Kalisky, B. et al. Locally enhanced conductivity due to the tetragonal domain structure in $LaAlO_{33}/SrTiO_3$ heterointerfaces. *Nat. Mater.* **12**, 1091–1095 (2013).
38. Ma, E. Y. et al. Mobile metallic domain walls in an all-in-all-out magnetic insulator. *Science* **350**, 538–541 (2015).
39. Bachmann, M. D. et al. Spatial control of heavy-fermion superconductivity in ceirin$_5$. *Science* **366**, 221–226 (2019).
40. Yang, F. et al. Nematic transitions in iron pnictide superconductors imaged with a quantum gas. *Nat. Phys.* **16**, 514–519 (2020).
41. Kalisky, B. et al. Stripes of increased diamagnetic susceptibility in underdoped superconducting $Ba(Fe_{1-x}CO_x)_2As_2$ single crystals: evidence for an enhanced superfluid density at twin boundaries. *Phys. Rev. B* **81**, 184513 (2010).
42. Aharon-Steinberg, A. et al. Long-range nontopological edge currents in charge-neutral graphene. *Nature* **593**, 528–534 (2021).
43. McCormick, K. L. et al. Scanned potential microscopy of edge and bulk currents in the quantum Hall regime. *Phys. Rev. B* **59**, 4654–4657 (1999).
44. Rosen, I. T. et al. Measured potential profile in a quantum anomalous Hall system suggests bulk-dominated current flow. *Phys. Rev. Lett.* **129**, 246602 (2022).
45. Lian, B., Sun, X.-Q., Vaezi, A., Qi, X.-L. & Zhang, S.-C. Topological quantum computation based on chiral majorana fermions. *Proc. Natl Acad. Sci. USA* **115**, 10938–10942 (2018).
46. Okazaki, Y. et al. Quantum anomalous Hall effect with a permanent magnet defines a quantum resistance standard. *Nat. Phys.* **18**, 25–29 (2022).

Methods

Sample growth and sample fabrication

We used a VEECO 620 molecular beam epitaxy (MBE) system to grow heterostructures comprising three-QL $Cr_{0.15}(Bi,Sb)_{1.85}Te_3$, five-QL $(Bi,Sb)_{1.85}Te_3$ and three-QL $Cr_{0.15}(Bi,Sb)_{1.85}Te_3$ on STO (111) substrates (MTI Corporation). Cr composition was nominal (based on past calibrations). STO substrates were cleaned using deionized water at 90 °C for 1.5 h and thermally annealed at 985 °C for 3 h in a tube furnace with flowing oxygen gas. The substrate was outgassed under vacuum at 630 °C for 1 h and then cooled to 340 °C for heterostructure growth. When the substrate temperature was stable at 340 °C, high-purity Cr (5N), Bi (5N), Sb (6N) and Te (6N) were evaporated from Knudsen effusion cells to form the heterostructure. The desired beam equivalent pressure (BEP) fluxes of each element and growth rate were precisely controlled by cell temperature. The BEP flux ratio of Te:(Bi + Sb) was kept above ten to prevent Te deficiency. The BEP flux ratio of Sb:Bi was kept around two to tune the chemical potential of the heterostructure close to the charge neutrality point. Heterostructure growth rate was 0.25 QL min^{-1}, and pressure in the MBE chamber was maintained at 2×10^{-10} mbar during growth.

Following growth, heterostructures were fabricated into a $200 \times 75\ \mu m^2$ Hall bar and a two-terminal sample using photolithography. Sample shape was defined by argon plasma etching. Following etching, 10 nm Cr/60 nm Au was deposited outside the active area of the Hall bar to make electrical contact. The top gate was fabricated by depositing a 40 nm Al_2O_3 layer via atomic layer deposition across the entire sample and evaporation of a 10 nm Ti/60 nm Au layer patterned by optical lithography.

Electrical connections and measurements

Electrical connection to the samples was made via thermocoax lines in a cryogen-free dilution refrigerator with a base temperature of 15 mK at the mixing chamber plate. Samples were mounted on a high-thermal-conductivity copper cold finger in the bore of a 6 T–1 T–1 T vector magnet. A ruthenium oxide thermometer confirmed that the sample stage had cooled to at least 45 mK, which is the lowest calibrated temperature reading.

Measurements of R_{yx} and R_{2T} of the Hall bar were carried out using standard lockin measurements with the contact configurations shown in Extended Data Fig. 1. A sinusoidal a.c. bias was applied to the sample. The current was monitored with an Ithaco current preamplifier and an SR830 lockin amplifier. Voltage drops were amplified by an SR560 preamplifier with an input impedance of 100 MΩ and read out with an SR830 lockin amplifier. For the measurements shown in Fig. 1d a frequency of 11.3 Hz was used, resulting in a phase difference between excitation and signals below 5°. For transport measurements corecorded with magnetic imaging a lockin frequency of 140.5 Hz was used, resulting in a phase shift of approximately 10°. The higher frequency notably improved the noise performance of the SQUID. Voltage across the sample to determine R_{2T} was measured at room temperature. We subtracted 300 Ω from all R_{2T} values to account for the 300 Ω resistance of the wiring in the cryostat. Although our sample was patterned into a six-terminal Hall bar geometry, contacts on the right side of the sample were shorted on-chip leaving us with four independent contacts instead of the usual six, as shown in Extended Data Fig. 1. In addition to R_{yx} and R_{2T}, we measured the longitudinal resistance of the sample using geometric symmetrization[47]. Specifically, we show $R_{xx} = \frac{1}{2}\left(R_{14,23'} + R_{23',14}\right)$ in Extended Data Fig. 1e. Here, $R_{ij,kl} = V_{kl}/I_{ij}$ the current flowing from contact j to i and V_{kl} the voltage between contacts l and k. This R_{xx} is proportional to the longitudinal resistivity times of a geometric factor that is independent of V_{BG}.

Scanning SQUID microscopy

The scanning SQUID sensor has the same gradiometric layout as that described in ref. 15, with a pickup loop of 1.5 µm inner diameter. The SQUID is coupled to a SQUID-array amplifier mounted on the mixing chamber plate of the dilution refrigerator. We used a home-built piezoelectric scanner to scan the SQUID ~1 µm above the sample surface. To measure the flux signal produced by current flowing through the sample, we excited one of the sample contacts with an a.c. voltage to source a current between 10 and 50 nA at a frequency $f = 140.5$ Hz. We measured our devices under a variety of bias conditions and, in general, sourced a current $I(t) = I_{d.c.} + I^p_{a.c.}\sin(2\pi ft)$ through the sample. Throughout the manuscript we denote the peak amplitude of the oscillating current as $I^p_{a.c.}$ and define $I_{a.c.} = I^p_{a.c.}/\sqrt{2}$. The SQUID signal was then detected by a lockin amplifier that detects the RMS value of the flux at the first and second harmonic of the excitation frequency. As the two-terminal resistance of the sample changes with back-gate voltage, we adjusted voltage bias amplitude to maintain a constant current bias. To image dM/dV, a 140.5 Hz sinusoidal excitation with RMS ranging between 0.20 and 0.25 V was applied to the top gate with the source and drain contacts grounded. The SQUID signal was then detected with a lockin amplifier. For DC magnetic images, the SQUID signal was low-pass filtered and directly recorded.

Current and magnetization reconstruction

Because sample thickness was more than one order of magnitude smaller than both SQUID pickup loop radius and scan height, we treated both current density and magnetization as two-dimensional. The magnetic flux, $\Phi(x,y)$, at lateral position x, y at height z above the sample detected by SQUID was then given by convolution of the SQUID point spread function, K_{PSF}, and the appropriate Biot–Savart kernel, K_{BS}:

$$\Phi(x,y) = K_{PSF}(x,y) * K_{BS}(x,y) * g(x,y). \tag{1}$$

Here * denotes a convolution,

$$f(x,y) * h(x,y) = \int \mathrm{d}x'\,\mathrm{d}y' f(x',y')h(x'-x,y'-y). \tag{2}$$

The scalar function $g(x,y)$ can be interpreted as either magnetic dipole density, when reconstructing magnetization, or current stream function, which determines the two-dimensional current density through

$$\vec{j}(x,y) = \nabla \times [g(x,y)\hat{z}]. \tag{3}$$

In two dimensions, K_{BS} is given by

$$K_{BS} = \frac{\mu_o}{2\pi}\frac{2z^2 - x^2 - y^2}{(x^2 + y^2 + z^2)^{5/2}}. \tag{4}$$

We extracted K_{PSF} (shown in Extended Data Fig. 9) from images of superconducting vortices acquired using a nominally identical SQUID.

Reconstruction of $g(x,y)$ from a measured image $\Phi(x,y)$ with the inclusion of experimental noise is a deconvolution problem that requires regularization to avoid amplification of high spatial frequency noise. Here we write the problem as a linear system of equations that can then be solved directly. We combine K_{PSF} and K_{BS} into a single linear operator, M, such that equation (1) can be written as $\Phi = Mg$, where g is now a vector with length n equal to the number of pixels in an image and M is a $n \times n$ matrix. Given a suitably chosen regularization operator, Γ, that penalizes solutions that include high-frequency ringing, and regularization strength σ, we search for g^* that satisfies

$$g^* = \min_g 1/2\,\|Mg - \phi\|^2 + \sigma^2\,\|\Gamma g\|^2. \tag{5}$$

As such g^* is the best estimate of the true g and can be found by solving the linear equation

$$\left(M^TM + 2\sigma^2\Gamma^T\Gamma\right)g = M^T\phi. \tag{6}$$

M^T and Γ^T are the pseudo-inverse of M and Γ, respectively. In practice we do not directly calculate the elements of M but instead calculate the convolution Mg using fast Fourier transforms. Furthermore, we approximate M^T using the Wiener filter and choose the discrete Laplace operator as our regularization operator Γ.

For the one-dimensional line-cut data we utilize the same methods described above in one dimension. In this case, the SQUID point spread function and Biot–Savart kernel are integrated along one axis to form an effective one-dimensional point spread function.

Data availability

The data supporting the plots and findings of this paper are available at Zenodo: https://doi.org/10.5281/zenodo.8037337

References

47. Sample, H., Bruno, W., Sample, S. & Sichel, E. Reverse-field reciprocity for conducting specimens in magnetic fields. *J. Appl. Phys.* **61**, 1079–1084 (1987).

Acknowledgements

We thank C.-Z. Chang and P. L. McEuen for valuable discussions and C. Clement and J. P. Sethna for help with the reconstruction methods. Work at Cornell University was primarily supported by the US Department of Energy, Office of Basic Energy Sciences, Division of Materials Sciences and Engineering, under award no. DE-SC0015947. Sample synthesis and fabrication at Penn State was supported by the Penn State 2DCC-MIP under NSF Grant nos. DMR-1539916 and DMR-2039351.

Author contributions

K.C.N. conceived the experiment. K.C.N. and N.S. supervised the research. G.M.F. performed scanning SQUID microscopy, electrical transport measurements and data analysis. R.X. grew and characterized the magnetically doped topological insulator films and fabricated the devices with help from A.R.R. G.M.F. and K.C.N. wrote the manuscript with contributions from all authors.

Competing interests

The authors declare no competing interests.

Additional information

Extended data is available for this paper at https://doi.org/10.1038/s41563-023-01622-0.

Supplementary information The online version contains supplementary material available at https://doi.org/10.1038/s41563-023-01622-0.

Correspondence and requests for materials should be addressed to Katja C. Nowack.

Peer review information *Nature Materials* thanks the anonymous reviewers for their contribution to the peer review of this work.

https://doi.org/10.1038/s41563-023-01622-0

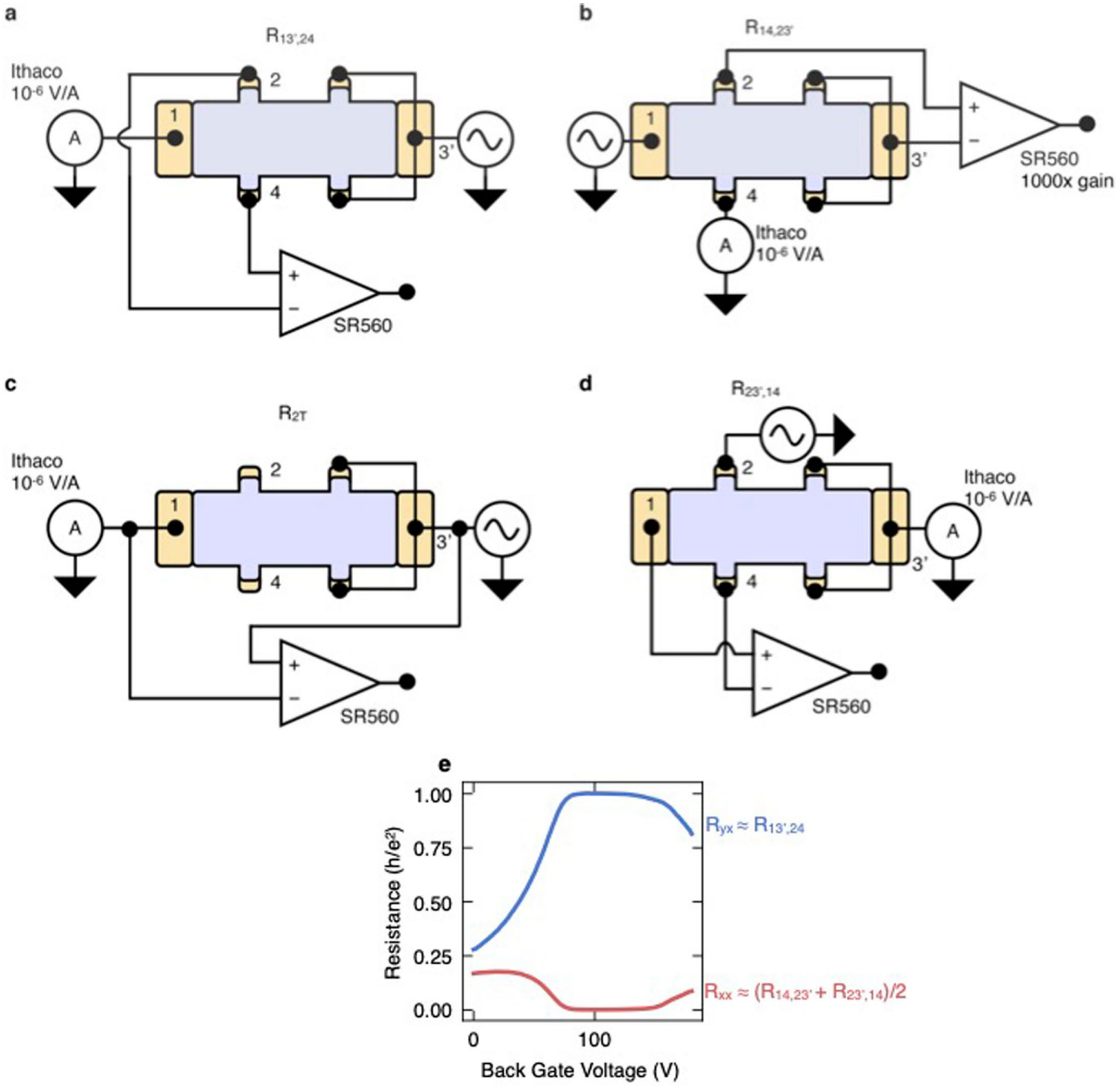

Extended Data Fig. 1 | Transport measurement configurations. Schematics showing the configurations to measure (a) R_{yx}, (c) R_{2T} and (b,d) the combinations needed to obtain R_{xx} interchanging current and voltage probes. (e) Hall resistance (R_{yx}, blue) as shown in Fig. 1d and longitudinal resistance (R_{xx}, red) measured as described in (b,d).

https://doi.org/10.1038/s41563-023-01622-0

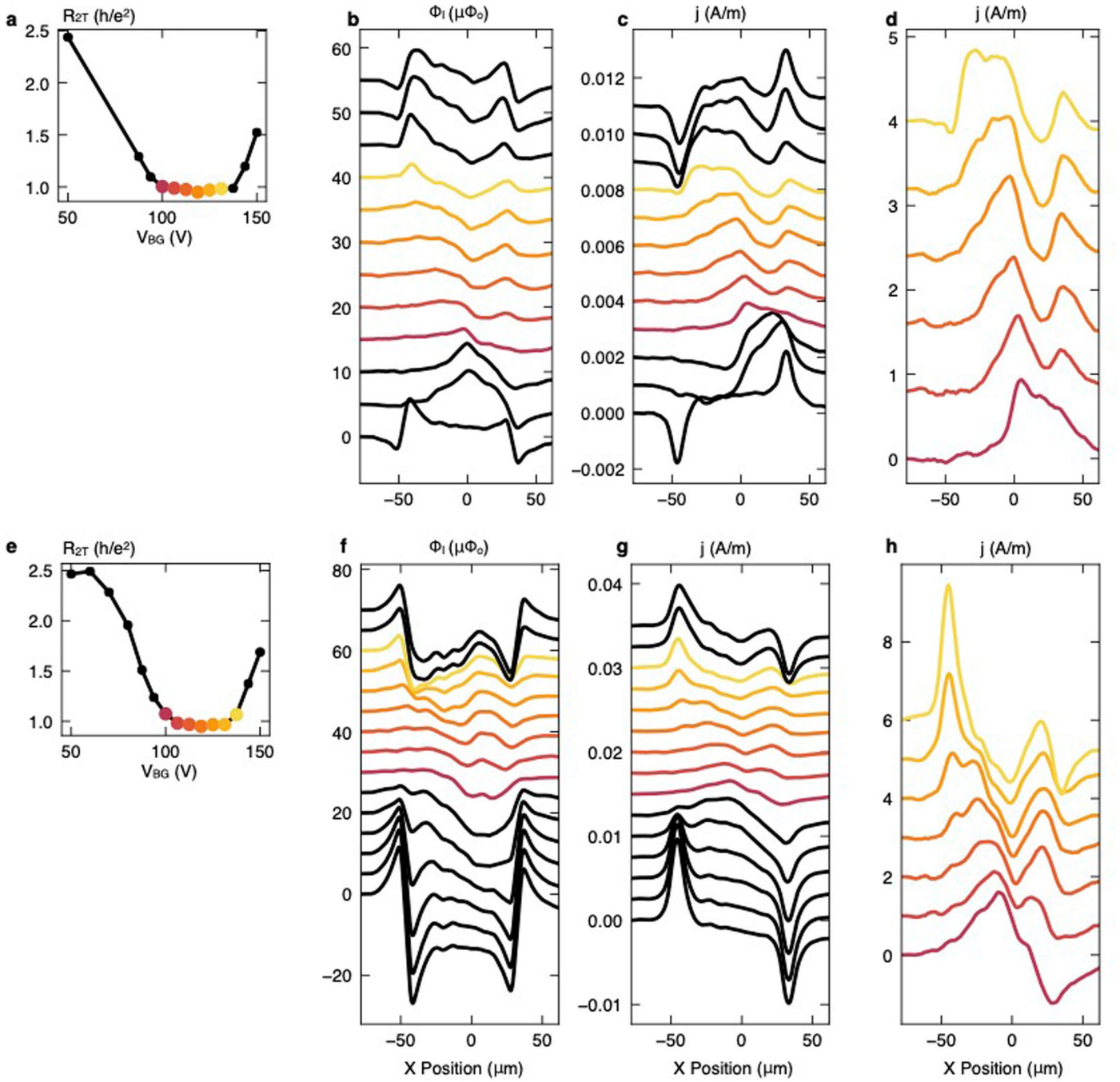

Extended Data Fig. 2 | Current imaging on the two-terminal sample. Imaging the current density on a two-terminal sample fabricated from the same thin film. (a) R_{2T} co-recorded with magnetic imaging versus V_{BG}. 300 Ω of wire resistance is subtracted. Color-coded points correspond to the colored traces. (b) SQUID flux, Φ_I, with $I_{a.c.}$ = 25 nA and I_{DC} = 0. The film is magnetized out of the plane. (c) Reconstructed current density from (b). (e) Reconstructed current density for V_{BG} range in which the two-terminal resistance is near quantization. (f-i) Same as (a-e) with a different sample configuration. The film is magnetized into the plane. We source $I_{a.c.}$ = 25 nA with a positive $I_{DC} = I^{p}_{a.c.} = 35.3$ nA.

https://doi.org/10.1038/s41563-023-01622-0

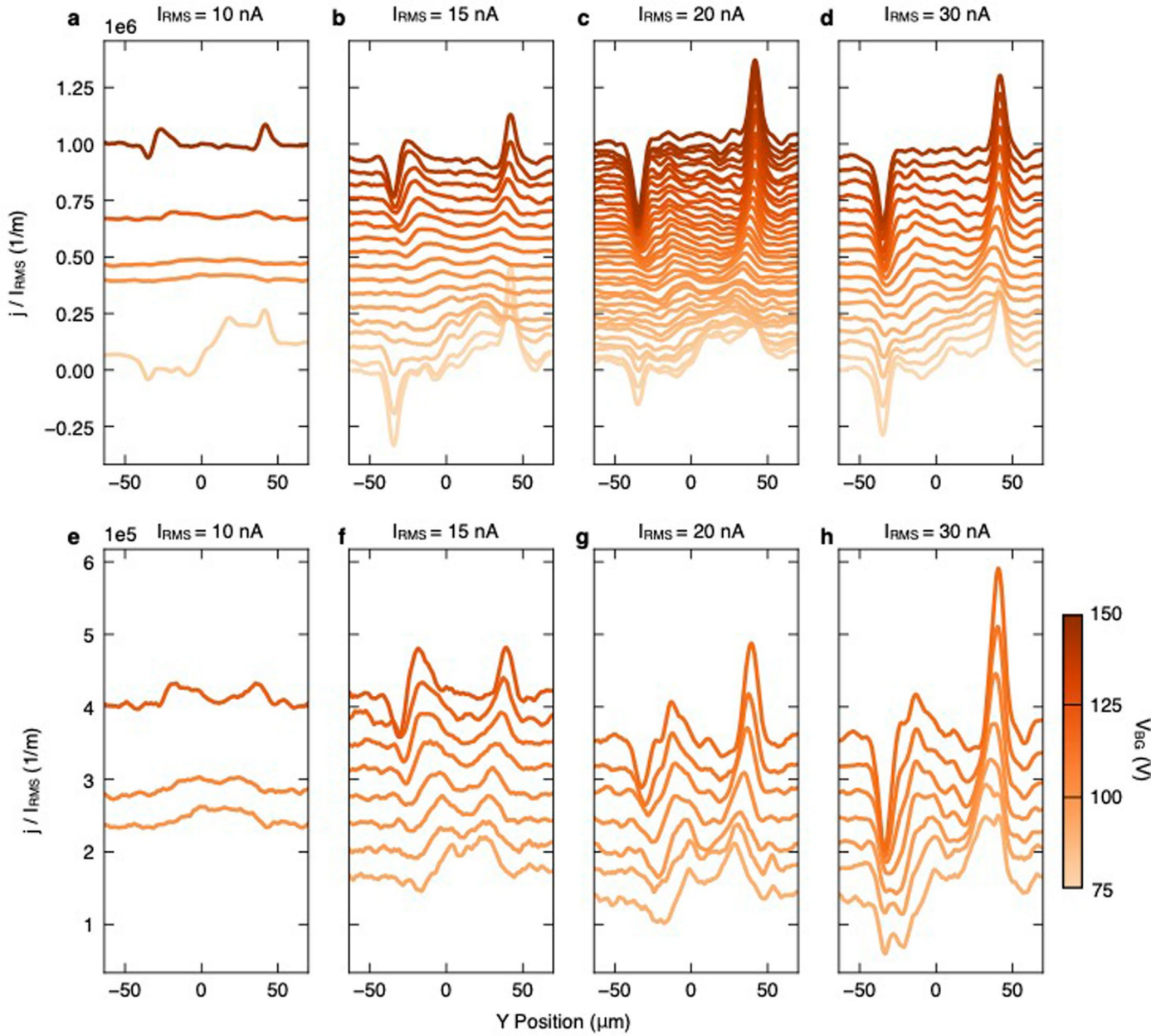

Extended Data Fig. 3 | Current reconstruction at different bias levels. Reconstructed current density normalized by $I_{a.c.}$ for different bias levels. The Hall bar is biased with a positive DC offset such that $I^{p}_{a.c.} = I_{d.c.}$. Traces are color-coded and offset vertically by the back-gate voltage for comparison. (a) $I_{a.c.}$ = 10 nA. (b) $I_{a.c.}$ = 15 nA, reproduced from figure 2. (c) $I_{a.c.}$ = 20 nA. (d) $I_{a.c.}$ = 30 nA. (e-h) same as (a-d) with, zoomed in on the V_{BG} corresponding to the QAH regime.

https://doi.org/10.1038/s41563-023-01622-0

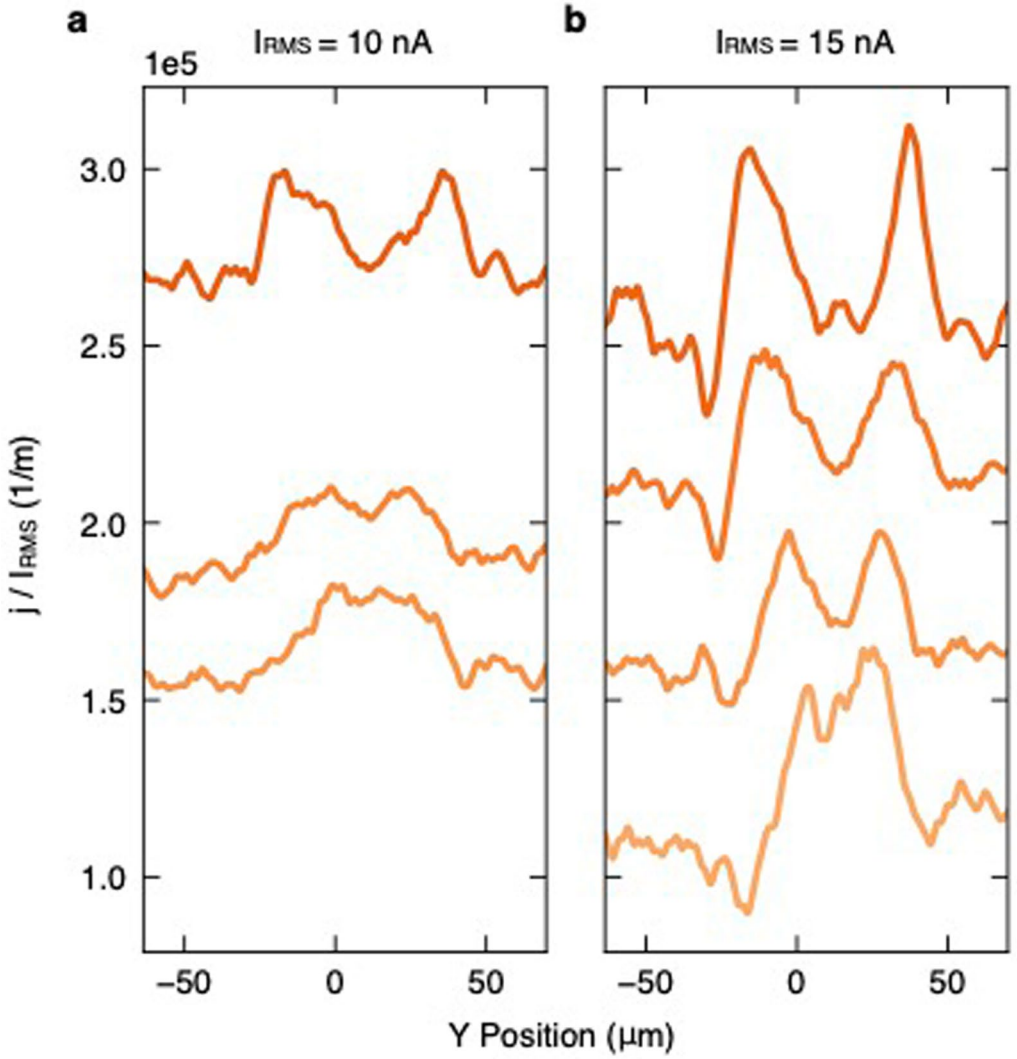

Extended Data Fig. 4 | Comparing data acquired at low bias currents. Same data as in Extended Data Fig. 3 but focusing on only low bias currents. Traces are color-coded and offset for clarity to indicate the back gate voltage. (a) $I_{a.c.}$ = 10 nA. (b) $I_{a.c.}$ = 15 nA. The V_{BG} corresponding to the center of the QAH regime is shifted by approximately 15 V between the two data sets (see Supplementary Section 2 for details).

https://doi.org/10.1038/s41563-023-01622-0

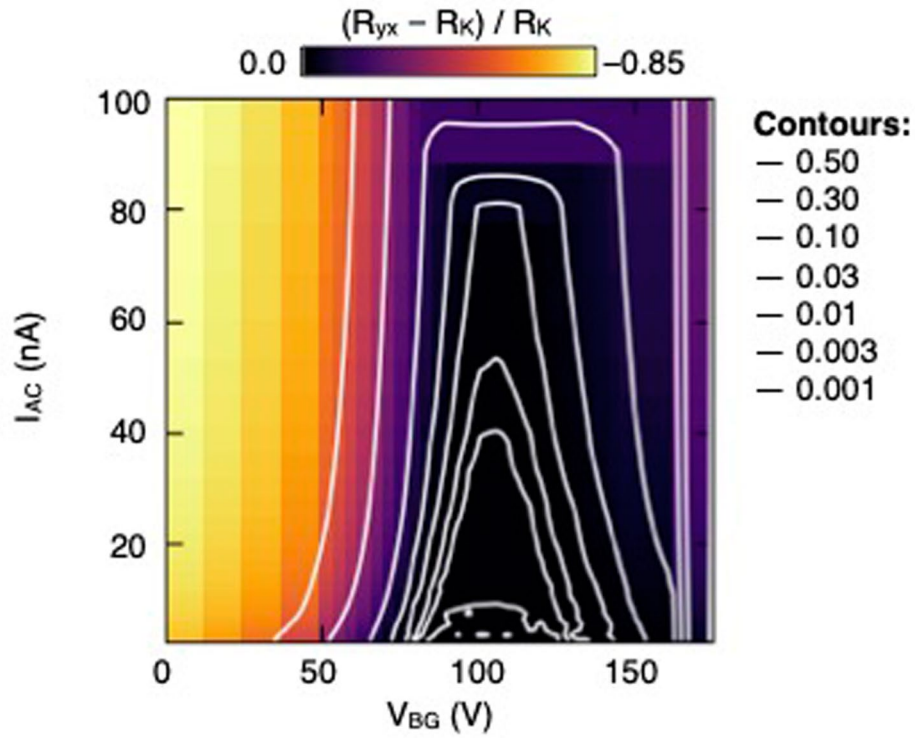

Extended Data Fig. 5 | Current bias dependence of the Hall resistance. Dependence of the Hall resistance on $I_{a.c.}$ current bias. Overlaid contours indicate the deviation from the quanitzed value as V_{BG} and bias current are adjusted.

https://doi.org/10.1038/s41563-023-01622-0

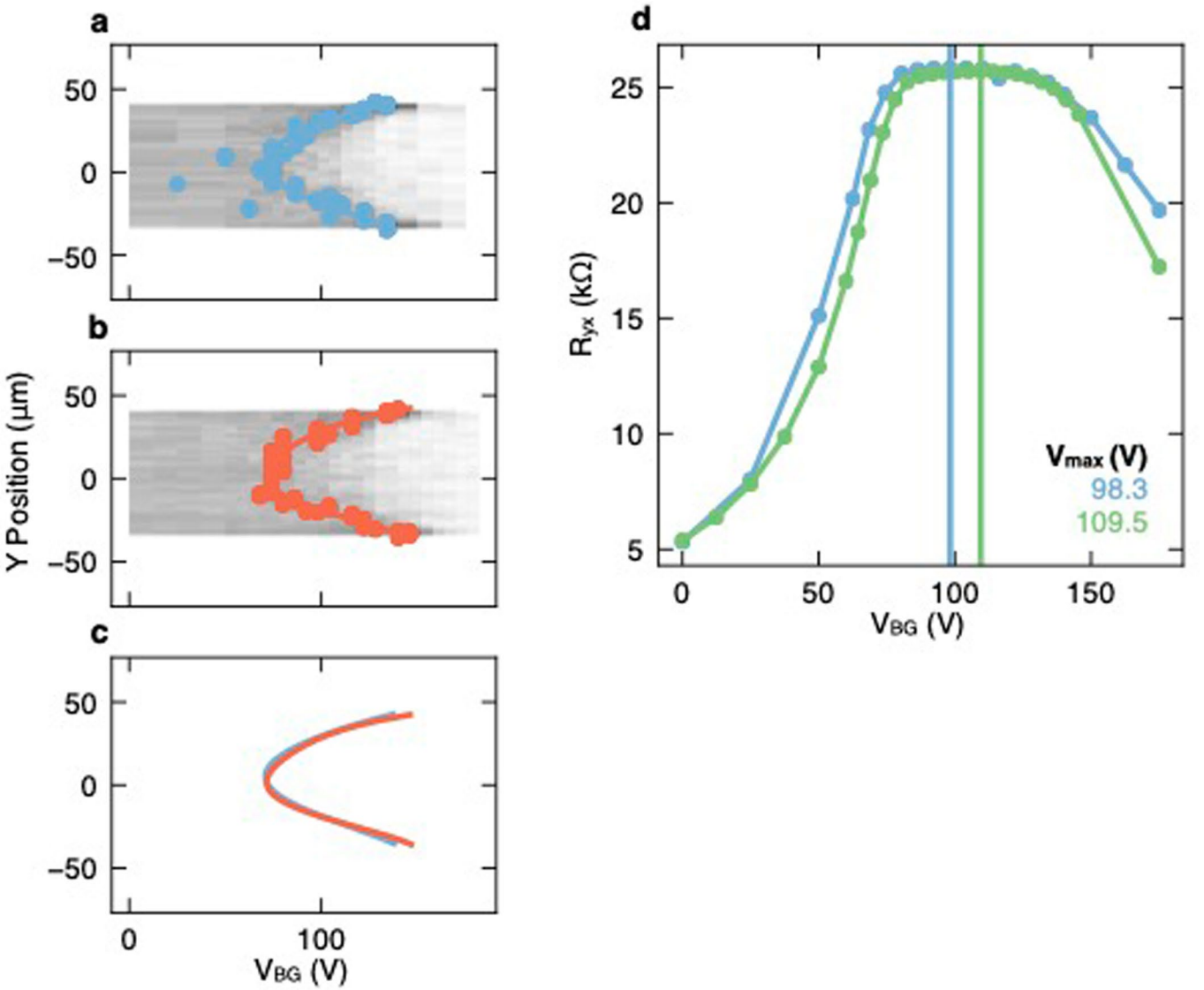

Extended Data Fig. 6 | Registration of different gate sweeps. (a) dM/dV_{TG} data with co-recorded measurements of R_{yx} versus V_{BG}. Blue points mark the minimum in dM/dV_{TG} for each position y along the channel. Blue curve is a 5th order polynomial fit to the points. (b) Same as (a) with for the dM/dV_{TG} data presented in Fig. 3 and 4a for which R_{yx} was not co-recorded. (c) Comparison of the polynomial fits in (a) and (b). Based on the alignment of the polynomial fits, we use the same V_0 for both dM/dV datasets. (d) Comparison of R_{yx} co-recorded with (a) and the current imaging data in Fig. 2b. R_{yx} measured with $I_{a.c.}$ = 15 nA and co-recorded with magnetic imaging data (green) compared to R_{yx} measured with $I_{a.c.}$ = 2.5 nA measured at each back gate voltage in the dM/dV data in figure (a) (blue). Vertical lines denote the gate voltages V_{Off} where R_{yx} is maximized. A difference of 11.2 V is observed between the two data sets. The two values V_{Off} are used for comparing data in Fig. 4a,b.

https://doi.org/10.1038/s41563-023-01622-0

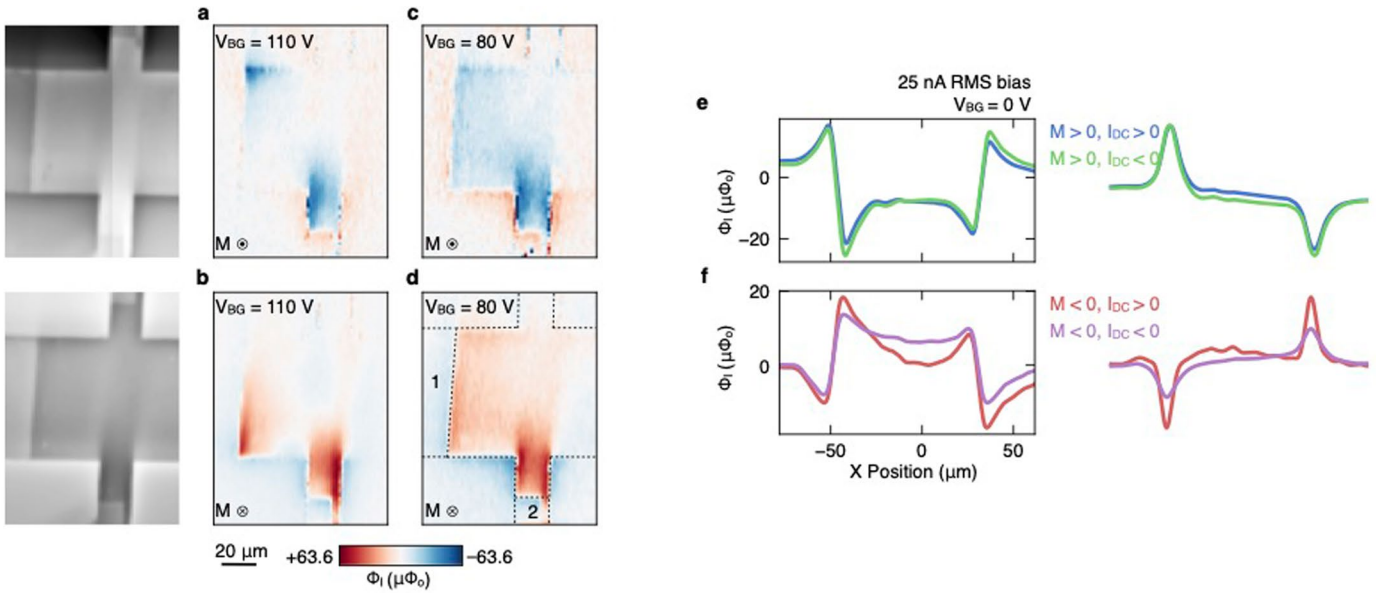

Extended Data Fig. 7 | Hot-spots and bias-induced heating. (a) Flux signal produced with $I_{a.c.}$ = 20 nA from contacts 1 to 2 (as indicated in (d)) with the sample gated into the quantized regime and the sample magnetized out of the plane. A strong signal is observed at the corners of the contacts. (b) Same as (a) with the static magnetization reversed. The location of the hot-spots changes and the sign of the signal is inverted. This is consistent with local demagnetization at the sample corners when the sample is gated into the quantum anomalous Hall regime. (c) Same as (a) with the sample gated away from the quantized regime. Signs of demagnetization are observed throughout the sample. (d) Same as (c) with the magnetization reversed. (e-f) Flux linecuts over the two terminal device gated far away from the quantum anomalous Hall regime with $I_{a.c.}$ = 25 nA bias current and $I_{d.c.} = I^{p}_{a.c.}$ with the sample magnetized out of the plane (e), and with the sample magnetized into the plane (f). The signals change sign with the magnetization direction and have a weak dependence on DC bias direction, indicating that they arise from a partial demagnetization of the sample rather than the transport current density.

https://doi.org/10.1038/s41563-023-01622-0

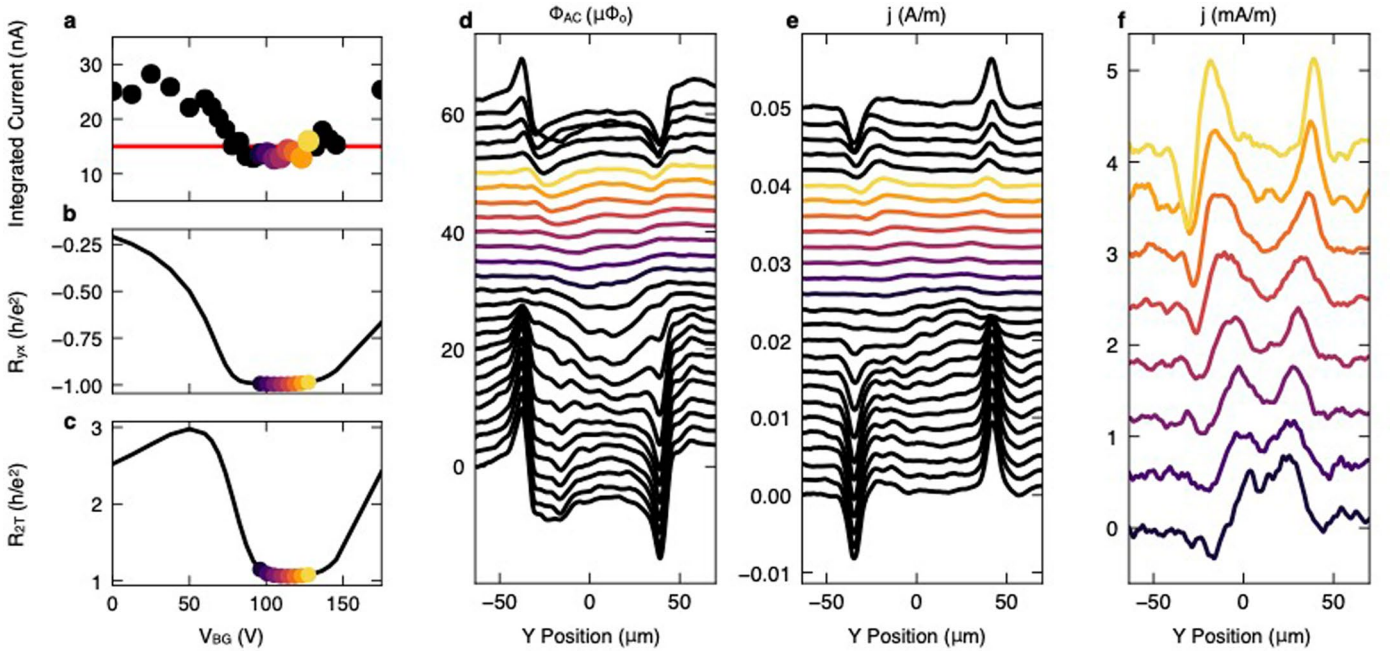

Extended Data Fig. 8 | Extended back gate voltage range for data shown in Fig. 2d and Fig. 4b. (a) Integral of the reconstructed current density, j_x over width of the Hall bar along y. Colors indicate line trace where the Hall resistance is closest to the quantized value. Red line indicated 15 nA, which is the bias current. Outside the quantized regime, we find deviations between the total reconstructed current and the applied current due to heating-induced signals as discussed in the main text. (b) R_{yx} and (c) R_{2T} versus V_{BG} co-recorded with the imaging. (d) SQUID flux detected over the channel as a function of back gate voltage. Color-coded traces correspond to data displayed in Fig 2. Traces in black are dominated by a partial demagnetization of the due to bias-induced heating. (e) Reconstructed current density for the traces in (e). (f) Color-coded traces from (e) re-plotted on a new y-scale.

https://doi.org/10.1038/s41563-023-01622-0

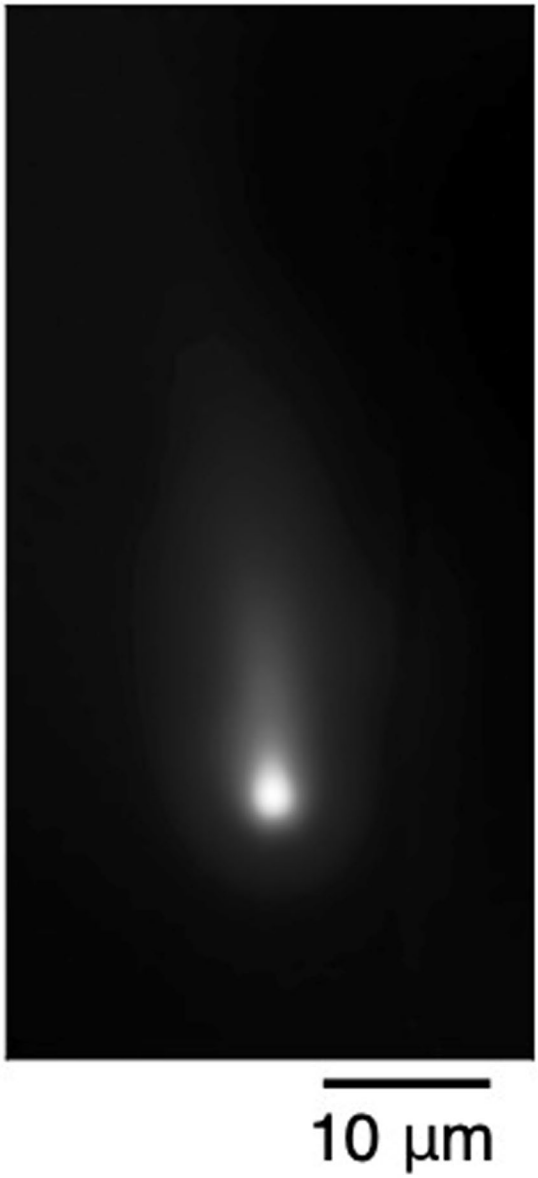

Extended Data Fig. 9 | SQUID point spread function. Image of the SQUID point spread function, K_{PSF} extracted from imaging a superconducting vortex. The SQUID pickup loop has an inner diameter of 1.5 μm, giving few-micrometer scale spatial resolution for magnetic imaging.